

Transient Evolution of Rheological Properties of Dense Granular Inertial Flow Under Plane Shear

Xuejie Zhang

Hefei University of Technology <https://orcid.org/0000-0001-6750-843X>

Wei Wang

Hefei University of Technology

Xiaojun Liu

Hefei University of Technology

Kun Liu (✉ liukun@hfut.edu.cn)

Hefei University of Technology

Research Article

Keywords: Rheology, Dense granular inertial flow, Transient, Internal friction coefficient, Shear strength

Posted Date: August 2nd, 2021

DOI: <https://doi.org/10.21203/rs.3.rs-735864/v1>

License: © ⓘ This work is licensed under a Creative Commons Attribution 4.0 International License.

[Read Full License](#)

Version of Record: A version of this preprint was published at Tribology Letters on March 7th, 2022. See the published version at <https://doi.org/10.1007/s11249-022-01578-3>.

Transient evolution of rheological properties of dense granular inertial flow under plane shear

Xuejie Zhang, Wei Wang, Xiaojun Liu, Kun Liu*

Institute of Tribology, School of Mechanical Engineering, Hefei University of Technology, Hefei, Anhui, 230009, China

*Corresponding author: Kun Liu, liukun@hfut.edu.cn

Abstract: Exploration on the transient evolution of the rheological properties of dense granular inertial flow is essential for revealing how the balance is established between the boundary drive strength and the internal shear strength. In this paper, discrete element method simulations are performed to study the transient flow characteristics of a dense granular system under plane shear in the inertial regime. To this end, we quantitatively analyze the changes in the system's flow state, interfacial friction coefficient, internal friction coefficient, and microstructure. Simulation results show that the evolution of the horizontal flow experiences three typical stages, namely transmission, adjustment, and stabilization. Meanwhile, the shear dilatancy caused by the vertical movement of particles, gradually loosens the filling state, weakens the spatial geometric constraint and the system's tangential load-bearing capacity, thereby decreasing the interfacial friction coefficient and reducing the boundary drive strength. On the other hand, the variations in the anisotropies of both contact orientation and contact forces, increase the internal friction coefficient and improve the internal shear strength. Therefore, the evolution of flow state from initially static to finally stable reduces the boundary drive strength while enhances the internal shear strength, and eventually a balance between them is achieved. Distinguished from the micromechanical behaviors, under different shear velocities the internal shear strength always mainly originates from the anisotropies in contact orientation and in normal contact force. Moreover, the contribution of the anisotropy in contact orientation becomes more predominant with the increase of shear velocity.

Keywords: Rheology; Dense granular inertial flow; Transient; Internal friction coefficient; Shear strength

1. Introduction

Under shear, granular materials exhibit fascinating properties capable of sustaining stress as a solid, or flowing as a fluid [1-3]. The granular flow has motivated many studies over the past decades, since the rheological properties of dense granular materials play an important role in various natural phenomena and industrial applications such as geographical faults, powder metallurgy, three-body friction, and particle flow lubrication [4-10]. Generally, three different granular flow regimes are categorized according to the flow state, including quasi-static regime, inertial regime, and collisional regime [11-14]. In the inertial regime, when a dense granular system is subjected to continuous shear, a local flow near the boundary is first generated after the initial static equilibrium is broken, and gradually a global flow will be achieved and maintained stable finally. Meanwhile, the shear flow is accompanied with dilatancy, which represents the volume expansion of the granular system [15-18]. Two representative quantities, i.e., the interfacial friction coefficient and the shear strength, are most commonly employed to characterize the rheological properties of dense granular flow [19-23]. The interfacial friction coefficient μ can be understood as the drive strength provided by the boundary for maintaining the particle flow, defined as the ratio of the shear stress τ on the shear boundary to the confining pressure P [21-26]. On the other hand, the shear strength of a granular material with respect to a specific plane inside the material and a given normal stress σ_n acting on it, is the maximum shear stress τ_p on that plane that the material can withstand before failure happens by shear deformation [27-29]. According to the Mohr-Coulomb yield criterion, τ_p is proportional to the normal stress σ_n for cohesionless materials, and the shear strength is typically characterized by the friction angle ϕ , defined as $\mu^* = \tan\phi = \tau_p/\sigma_n$ which is also referred to as the internal friction coefficient. Alternatively, the internal friction angle ϕ can be expressed in terms of stress invariants, given as $\sin\phi = q/p$, where q is the average stress and p is the stress deviator [13, 19, 30]. In the steady state, these two coefficients are approximately equal, and can be unified as the effective friction coefficient μ_e .

The interfacial friction characteristics could be influenced by several geometry factors, including the boundary surface structure, the thickness of particle layers, the shape and the constrained extent of particles [29-34]. Moreover, the interfacial friction coefficient μ has a significant dependence on the shear velocity and the applied load [35-37]. Most experimental studies on the interfacial friction characteristics deal with local shear deformation, where stick-slip or particle flow only occurs near the boundary due to either the small shear velocity or the short shear duration. However, when the boundary shear velocity is large and the shear time is long enough, the system will reach a stable flow state eventually. In the steady inertial flow state, the interfacial friction coefficient μ is a constant value and independent on the initial filling state of the dense granular system. For rigid dry granular materials, the flow state can be measured by the dimensionless inertia number I , which represents the ratio of the inertia force to the confining pressure [11, 38, 39]. Numerous experimental and simulation results have confirmed that, in the inertia regime, the interfacial friction coefficient μ monotonically increases as a function of the inertia number I [21-23, 39-41]. It is a familiar feature of granular rheology that the interfacial friction coefficient μ is closely related to the system's flow state during the shear process.

On the other hand, the interparticle contact and contact forces exhibit fabric anisotropies, which are the microscopic origins of the internal shear strength [13, 19, 42-44]. At the microscopic scale, particles transfer forces through interparticle contacts. The variation of flow state changes the contact status and the force transmission paths between particles, thereby altering the topology of the microscopic contact network and the characteristics of force chains [43-46]. As a result, the shear strength significantly changes during the inertial flow due to the temporal and spatial variations in the topology of the force chains. Currently, much attention has been paid to analyzing the granular shear strength under the static filling or the stable inertial flow situations. For the stationary granular system, the internal shear strength is independent on the size polydispersity of the filled particles [47-49]. In addition, the influences of the different particle shapes on the internal shear strength were also investigated [13, 29-31, 50-54].

As for the stable inertial flow state, Azéma *et al.* [13] compared the rheological properties of a frictionless granular system between pentagonal particles and circular discs. Binaree *et al.* [29] further explored the integrated effects of inter-particle friction and particle shape on the internal shear strength. Besides, the rheological properties and microstructure characteristics of some cohesive granular systems were investigated [41, 55-57], where the effect of viscosity on the internal shear strength was discussed.

By virtue of the above-mentioned studies, the steady rheological properties of dense granular materials have been well studied under the equilibrium condition, where the boundary drive strength is balanced with the internal shear strength. However, it is still not clear regarding how the balance between the two strength quantities is gradually established in the continuous shear process, which requires a dedicate investigation on the transient evolution of the rheological properties. The plane shear system is the most commonly used model for exploring the particle flow behaviors, owing to its simplicity in the composing structure and the motion manner. Additionally, under steady flow state, the flow velocity linearly increases along the height, which can be used as a criterion for judging whether the system reaches stable [58]. Discrete element method (DEM) serves as a powerful tool for studying the mechanical properties of granular materials, because it can extract the microscopic information of individual particles but also analyze the macroscopic behaviors of the whole granular system [59, 60]. Therefore, this paper employs DEM to analyze the transient flow process of a plane shear system, by carefully characterizing the evolution principles of the flow state, the mechanical behaviors, as well as the microstructure characteristics at different moments. Moreover, we clarify the influences of flow state on both the interfacial and internal friction coefficients, and finally reveal the relationship between the boundary drive strength and the internal shear strength. In addition, the influences of the shear velocity are explored.

2. DEM Model and theory

2.1 DEM method of plane shear

In the two-dimensional DEM model, the granular material is described as a collection of discrete discs. The contact force dependent on the force-displacement relationship between particles is defined by the soft contact method. The motion information of each particle is derived from its own unbalanced force using the Newton's second law. As shown in Fig. 1(a), the dense granular material is consisted by $N_p = 2 \times 10^4$ cohesionless rigid disc particles with an average diameter of $d = 1$ mm. The system's solid fraction is $\varepsilon = 0.84$. Initially, the system's length along x -axis is $L = 200d$, and the height along y -axis is $H = 96d$. Compared with similar studies, the number of particles consisted in this simulation model is large enough to ensure the statistical confidence of the analysis results. The particle size distribution polydispersity is set 20% to avoid crystallization. The top and bottom plates are rough boundaries formed by the bonding monodisperse particles with diameter d , while the side walls are periodic boundaries. During shear, the bottom plate is fixed, and the top plate slides tangentially at a constant velocity V_x and applies a constant normal stress P to the granular system.

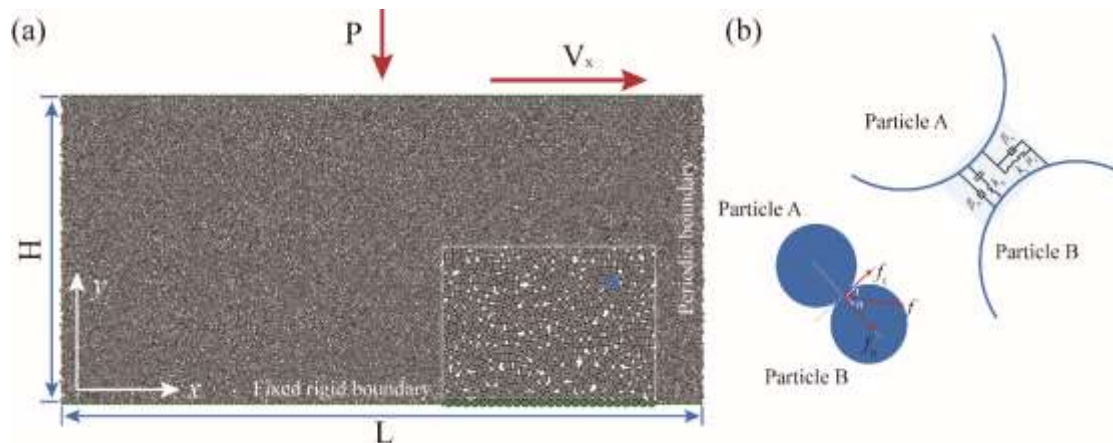


Fig. 1 (a) Two-dimensional DEM model of dense granular system under plane shear, (b) linear contact model between particles

For the cohesionless rigid particles, a linear contact model (spring-dashpot model) is

used to define the contact force between particles, as shown in Fig. 1(b). The linear model consists of two parts, namely a stiffness model and a slip model. The stiffness model provides a linear elastic relationship between contact force and relative displacement. The normal contact force F_c^n is composed by the normal linear force and the normal damping force, written as $F_c^n = F_{cl}^n + F_{cd}^n = k_n g_s + d_n \dot{g}_s$, where k_n is the normal contact stiffness, d_n is the normal damping coefficient, g_s is the surface gap between particles, and \dot{g}_s is the relative normal translation velocity. For dry granular materials, the normal contact force between particles is always compressive, so the equation $F_{cl}^n + F_{cd}^n \leq 0$ satisfies. The tangential contact force F_c^s is incrementally updated using $F_c^s = F_c^{os} + \Delta F_c^s$, $\Delta F_c^s = k_t \Delta \delta_s + d_t \Delta \dot{\delta}_s$, where k_t is the tangential stiffness, $\Delta \delta_s$ is the relative tangential displacement increment, d_t is the tangential damping coefficient, and $\Delta \dot{\delta}_s$ is the relative tangential translation velocity. The relative motion between particles follows the Coulomb relationship $|F_c^s| \leq \mu_c F_c^n$, where μ_c is the sliding friction coefficient between particles, dictating that only when the equal sign is satisfied, relative sliding between particles is allowed.

2.2 Parameters setup

A series of dimensionless parameters related to the particle material properties and the shear conditions are set according to the references [38, 43], which mainly include the contact stiffness coefficient k , the stiffness ratio s , and the restitution coefficient e . The dimensionless contact stiffness coefficient $k = k_n/P$ measures the rigidity of particle and limits the maximum deformation of particle under external load, where P is the applied normal stress, and k_n is the normal contact stiffness. In detail, a large value of k represents rigid particles and a small value represents soft ones. Relevant studies have shown that once k exceeds 10^4 , it will no longer influence the results because rigid particles are ensured [21, 61]. Therefore, k is set to 10^4 herein. The stiffness ratio $s = k_t/k_n$ takes an empirical value of 0.5. The normal and tangential damping coefficient d_n and d_t are only related to the restitution coefficient e once the stiffness coefficient k_n and the stiffness ratio s are determined, that is, $d_n =$

$2\beta_n\sqrt{mk_n}$, and $d_t = 2\beta_s\sqrt{msk_n}$, where β_s and β_n are normal and shear critical-damping ratios, and $\beta_s = \beta_n = -\ln(e) / (\pi^2 + (\ln(e))^2)$. The restitution coefficient e determines the threshold value for granular system transforming from dense flow to dilution collision [11]. In order to broaden the range of inertial flow, e is set as a fixed value of 0.1. The particle-particle and particle-wall friction coefficients are both set to 0.4 and notated as μ_c . A combined set of $e = 0.1$ and $\mu_c = 0.4$ is frequently used in simulations, because it results in a strong dissipative granular system which well matches the real situation. The detailed parameters of granular system are listed in Tab.1.

Tab.1 The detailed parameters of granular system

Parameter	Symbol	Value
Number of particles	N_p	20000
Average particle diameter (m)	d	1×10^{-3}
Polydispersity		± 0.2
Particle density (Kg/m ³)	ρ	2210
System width (m)	W	0.2
Initial system height (m)	H	0.096
Coefficient of friction	μ	0.4
Coefficient of restitution	e	0.1
Stiffness ratio	s	0.5
Contact stiffness number	k	10^4
Normal stiffness (N/m)	k_n	5×10^5
Tangential stiffness (N/m)	k_t	2.5×10^5

Based on the range of the inertial number $I = \dot{\gamma} \frac{d}{\sqrt{P/\rho}}$, the flow state of granular materials can be categorized into three regimes, namely quasi-static regime ($I < 10^{-4}$), inertial regime ($10^{-4} < I < 10^{-1}$), and collisional regime ($I > 10^{-1}$) [23], where $\dot{\gamma}$ is the shear rate, d is the mean particle diameter, P is the normal stress, and ρ is the particle density. In this study, P is a fixed value of 50 Pa, and the shear velocity of the top plate is selected within the range of 0.01 m/s ~ 1.5 m/s, resulting in an inertial flow with I in the range of $6 \times 10^{-4} \sim 0.1$. DEM adopts an explicit numerical scheme in the calculation process, where the Newton's second law needs to be repeatedly called to update the particle's position and inter-particle contact information. During the

simulation process, the instantaneous micromechanical information is obtained by an interval of every 1000 steps, including particle's position and velocity, contact position and contact force, in order to monitor the evolution of flow state and multi-scale mechanical behaviors.

2.3 Calculation methods of friction coefficients

Here we clarify the calculation methods of the interfacial friction coefficient μ and the internal friction coefficient μ^* . For the plane shear system, the interfacial friction coefficient μ is the ratio of the total tangential force F_T to the total normal force F_N at all contact points between the top plate and the top layer particles,

$$\mu = \frac{F_T}{F_N} = \frac{\sum_{c \in B} f_c^t}{\sum_{c \in B} f_c^n} \quad (1)$$

where f_c^t and f_c^n are the tangential force and the normal force on a single contact point, and $c \in B$ represents the collection of contacts between particles and the top plate.

Based on the stress-force-fabric relationship proposed by Rothenburg [62], we conduct a statistical analysis on the distribution functions of contact orientation, normal contact force, and tangential contact force in polar coordinates, denoted as $P(\theta)$, $f_n(\theta)$, and $f_t(\theta)$, respectively, where θ is the angle of unit vector \mathbf{n} along the contact direction. These distribution functions provide abundant micromechanical information for accurately evaluating the anisotropy extent of granular system. Commonly, the first-order Fourier approximations are employed to describe them:

$$P(\theta) \cong 1/2\pi \{1 + a_c \cos 2(\theta - \theta_c)\} \quad (2a)$$

$$f_n(\theta) \cong \bar{f}_n \{1 + a_n \cos 2(\theta - \theta_n)\} \quad (2b)$$

$$f_t(\theta) \cong -\bar{f}_n a_t \sin 2(\theta - \theta_t) \quad (2c)$$

where a_c represents the anisotropy in contact orientation which is proportional to the difference in the number of directional contacts between along the maximum and along the minimum principal stress, a_n and a_t describe the directional variation of contact forces and reflect the load-bearing capacity of granular system, and θ_c , θ_n , and θ_t

are the corresponding privileged directions. These parameters give an approximate expression for the internal friction coefficient μ^* :

$$\mu^* \cong \frac{1}{2}(a_c + a_n + a_t) \quad (3)$$

This equation explains the source of the internal shear strength of granular system under plane shear.

3. Evolution of the flow state

In this part, we employ the simulation results of $P = 50$ Pa and $V_x = 0.5$ m/s as demo to quantitatively analyze the change of flow state and shear deformation. The flow state is characterized by the distribution profiles of both the horizontal and the vertical velocities of particles in the same layer along the system's height. Specifically, the horizontal velocity reflecting the rate of shear deformation is the main movement characteristic of particles, and the vertical velocity is used to analyze the dilatancy phenomenon.

3.1 Horizontal flow velocity

Fig. 2(a) shows the horizontal velocity distribution contours of all the particles within the system at six different moments in the evolution process. Overall, under continuous shear the local flow near the top plate is transferred downward layer by layer, then gradually expands into the whole system, and finally a global steady flow is formed. The horizontal velocity decreases from top layer to bottom layer, which is the result of energy dissipation caused by inter-particle friction and inelastic collisions. Here, the system's height is represented by the particle layer number L_p , $L_p = H_t/d$, where H_t is the instantaneous height measuring from the bottom plate to the top plate, and d is the average particle diameter. In Fig. 2(b), the average horizontal velocity of particles in the same layer is plotted in solid line as a function of the layer number, meanwhile the original data of the horizontal velocities of all the particles are scattered in gray shadow. The fluctuation represented by the width of the gray shadow is inevitable in the horizontal velocity, because of the inherent discrete nature of granular materials.

Nevertheless, it is observed that the fluctuation is relatively small and uniform throughout layers except for the area near the top plate. The evolution of horizontal velocity profile can directly reflect the change of flow status. During the time interval from 0.1 s to 6.5 s, the flow region expands from the local area near the top plate to the global system, besides, the horizontal velocity of the already flowing region gradually increases. Subsequently, the system at 6.5 s displays a global flow but still requires an adjustment process before reaching a steady flow at 27 s. Therefore, according to the shape change of the horizontal velocity profiles in Fig. 2(b), the evolution process of flow status experiences three stages, namely transmission (T), adjustment (A), and stabilization (S).

On the other hand, the whole system can be simply divided into two sections, i.e., flow region and non-flow region, written as $H_t = H_{tF} + H_{tS}$, where H_{tF} is the height of the flow region, and H_{tS} is the height of the non-flow region. Notably, H_t is a variable related to the flow state. We further normalize the heights by using $DH_F = H_{tF}/H_t$, and $DH_S = H_{tS}/H_t$. As shown in Fig. 2(c), during the transmission stage DH_F rapidly increases from 0 to 1, and correspondingly DH_S decreases from 1 to 0. During the adjustment and stabilization stages, the granular system always maintains a global flow state, so $DH_F = 1$, and $DH_S = 0$.

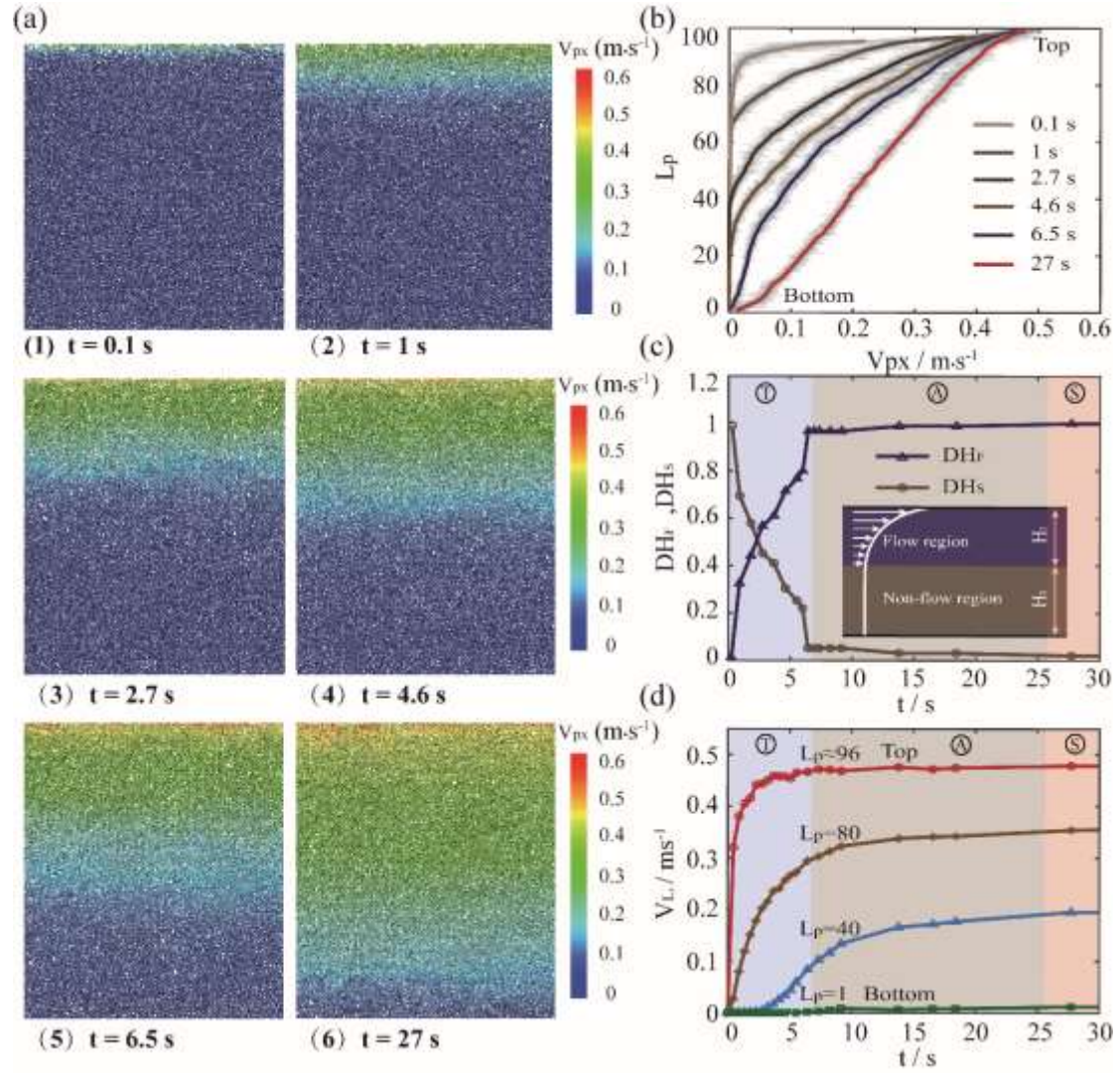


Fig. 2 Evolution process of the system's horizontal flow state under $P = 50$ Pa and $V_x = 0.5$ m/s, (a) the horizontal velocity distribution contours at six different moments, (b) the average horizontal velocity of particles in the same layer (in solid line), and the original data of the horizontal velocities of all the particles (in gray shadow), (c) time history plots of the normalized heights of the flow region DH_F and the non-flow region DH_S , (d) time history plots of the average horizontal velocity at four representative layers

Fig. 2(d) shows the time history plots of the average horizontal velocity at four representative particle layers which are the top layer ($L_p = 96$), the bottom layer ($L_p = 1$), and two middle layers ($L_p = 40$, and $L_p = 80$). The horizontal velocity gradually increases to a constant value for all the selected layers. In addition, the change of

velocity can reflect the evolution process of the system's flow state. When $V_{96} \neq 0$ and $V_1 = 0$, the system is in the flow transmission stage. Once $V_1 \neq 0$, transmission ends and then adjustment begins. When the velocities of the four particle layers reach constant, the granular system enters into the steady flow stage. Comparing the evolution characteristics, it is found that the closer to the top plate, the shorter time is required for the particle layer to reach a stable state. In other words, the growth rate of the horizontal velocity decreases from top to bottom, which is caused by the layer-by-layer attenuation of shear momentum.

3.2 Vertical velocity and dilatancy

Dilatancy is the volume expansion observed in granular materials when they are subjected to shear deformation. Fig. 3 illustrates the shear dilatancy mechanism of dense granular flow. Initially, the particles are related to each other through contacts and form a dense packing with the maximum solid fraction, as shown in Fig. 3(a). When the solid fraction is larger than a critical value, namely the jamming point, a preliminary dilation is necessary for shear deformation to occur. In other words, if the system's height undergoing shear remained fixed, the granular system would be blocked. In order to avoid blockage, the volume has to be expanded. As shown in Fig. 3(b), when sheared by the top plate, particles in the flow region cross over the peaks and valleys formed by the neighboring particles, causing the microscopic arrangement of particles. Whether a particle is crossing over peak or valley is indicated by the sign of the particle's vertical velocity. It is noteworthy that a particle could repeatedly cross over peaks or fall into valleys during the evolution process. Moreover, as the horizontal velocity increases, the duration for a particle horizontally moving over a valley is shortened, hence the vertical distance falling into the valley is reduced, leading to an increase in dilatancy.

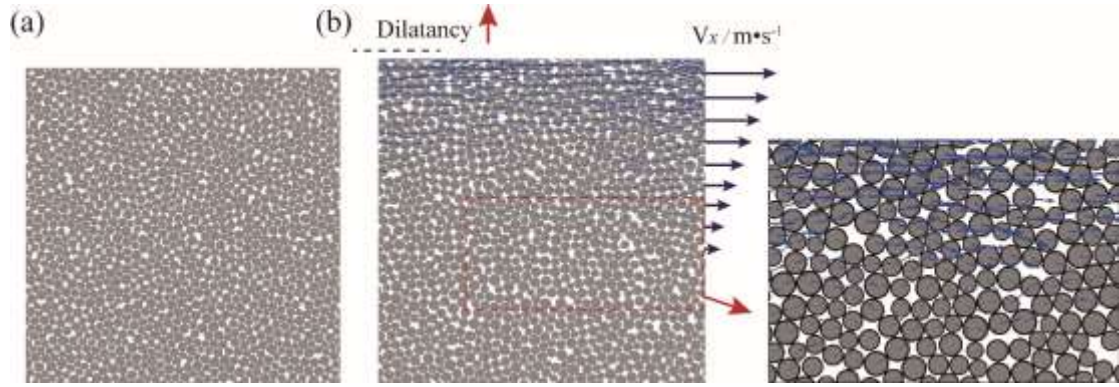


Fig. 3 Illustration of shear dilatancy in a dense granular system: (a) the initial dense packing state, (b) the movement of particles under shear

Fig. 4 shows the vertical velocity distribution contours of all the particles at six different moments in the evolution process. Additionally, the arithmetic average vertical velocity of particles in the same layer along the height direction is plotted on the right side for each moment, in order to quantify the dilatancy characteristics. First, it is observed that the upward and downward moving particles randomly coexist within the system, and the vertical movement gradually propagates from top to bottom. At $t = 0.0001$ s, the average vertical velocity is positive over the entire height, suggesting that the granular system dilates globally. In particular, the particles near the top plate expand rapidly under shear. Soon after that, the global dilatation is locally replaced as shown at $t = 0.1$ s. At $t = 1$ s and $t = 2.7$ s, the dilating region mainly resides near the top plate ($L_p > 80$), as the current dilatancy mainly comes from the local shear flow of particles. At $t = 4.6$ s, the maximum velocity has been transferred from near the top plate ($L_p > 80$) to the middle part ($L_p = 50 \sim 80$), which implies that the dilating region is moving down due to the propagation of local flow. Moreover, the sign of the average vertical velocity near the top plate changes from positive to negative. After the system reaches a stable state ($t = 27$ s), the shear dilatancy phenomenon totally disappears, because the average vertical velocity approaches to almost zero over the entire height.

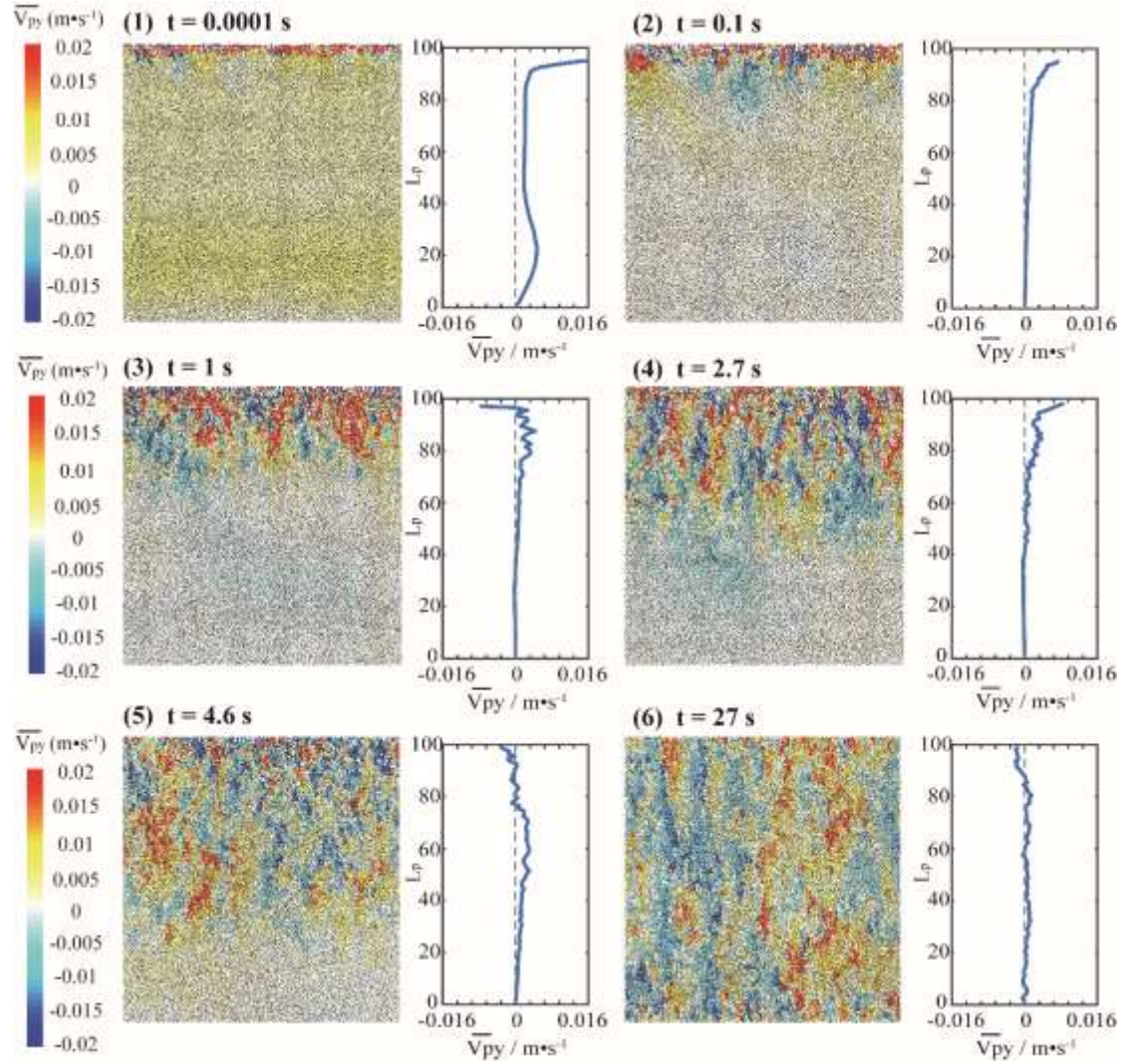


Fig. 4 The vertical velocity distribution contours of all the particles at six different moments, and the arithmetic average vertical velocity of particles in the same layer along the height direction under $P = 50$ Pa and $V_x = 0.5$ m/s

4. Evolution of interfacial friction coefficient and shear strength

4.1 Interfacial friction coefficient

This part still uses the simulation results under the conditions of $P=50$ Pa and $V_x = 0.5$ m/s to analyze the evolution of the boundary drive strength. Fig. 5 shows the time history plots of the tangential force F_T , the normal force F_N , and the interfacial friction coefficient μ , all of which act upon the top plate. In order to maintain the applied external load constant throughout the evolution process, the position of the top plate

must be dynamically adjusted. In detail, once the normal force F_N on the top plate exceeds 10 N, the top plate slightly moves upward to reduce the normal force, and vice versa. Therefore, as shown in Fig. 5(a), the normal force F_N always fluctuates around 10 N. Additionally, the fluctuation extent is closely related to the flow state, in the way that the fluctuation is intensive in the transmission stage (T) but mild in the adjustment (A) and stabilization (S) stages. As previously discussed, the particle flow state near the top plate changes dramatically at the beginning of the shear, and the horizontal and vertical velocity increases rapidly. Under this state, the particles collide violently with the top plate, resulting in large fluctuations in the normal and tangential forces. After that, the particle flow state changes smoothly, so the fluctuations gradually stabilize.

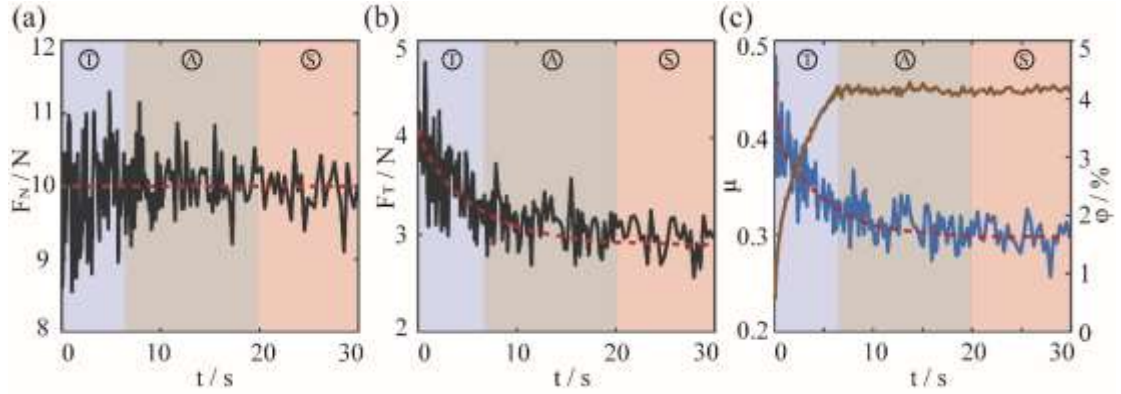


Fig. 5 The time history plots of the tangential force F_T (a), the normal force F_N (b), and the interfacial friction coefficient μ on the top plate (c), respectively, where $P = 50$ Pa and $V_x = 0.5$ m/s

In Fig. 5(c), the interfacial friction coefficient μ is calculated based on the results of F_N and F_T in Figs. 5(a) and 5(b). The dilatancy extent is also plotted on the right axis to investigate its influence on the interfacial friction. The dilatancy extent is measured by the expansion of the top plate's height, $\phi(t) = \frac{H_t - H_0}{H_0} \times 100\%$, where H_0 is the initial height, and H_t is the height at time t . First, it is found that the interfacial friction coefficient μ gradually decreases to a constant value during evolution. By contrast, $\phi(t)$ mainly increases in the transmission stage (T), and remains the maximum value afterwards. In the transmission (T) stage, dilatancy loosens the system's spatial

geometric constraint thus weakens the tangential load-bearing capacity, making the interfacial friction coefficient μ drop rapidly, which can be understood as the strain softening of granular material. However, in the adjustment (A) and stabilization (S) stages, the flow velocities within the particle layers change very slightly, so the shear dilatancy rate is close to zero, and the interfacial friction coefficient μ also tends to be a constant value.

4.2 Spatial distribution of the contact force network

Since the internal shear strength of granular system mainly comes from the anisotropies in the contact orientation and in the contact forces, it is necessary to get a picture of their spatial distributions first. Fig. 6(a) clearly presents the contact force network graphs at six different moments under the conditions of $P = 50$ Pa and $V_x = 0.5$ m/s. Here, the existence of an inter-particle contact is represented by a line segment connecting the center of the two contact particles, and the force magnitude f_c is proportional the line thickness. Furthermore, these contacts can be grouped into strong contact and weak contact by using the following rule: if the force magnitude f_c of a given contact is greater than the average value of all the contact force magnitudes $\langle f_c \rangle$, this contact is defined as a strong one; otherwise, it is defined as a weak contact. In the beginning of the evolution process ($t = 0.1$ s), the contact forces are small in most region except the local area near the top plate. Moreover, most of the strong contacts are sparsely scattered, thus cannot constitute a strong force chain structure. The strong force chains are the load-bearing carriers of granular system and are very sensitive to the change of flow state. In the subsequent transmission (T) stage (0.1 s ~ 6.5 s), more strong contacts appear and develop from near the top plate to the entire granular system, meanwhile they gradually connect with each other and constitute more strong force chains. In the stable state ($t = 27$ s), strong and right-tilted force chains are distributed within the system to carry the applied load and resist the shear deformation.

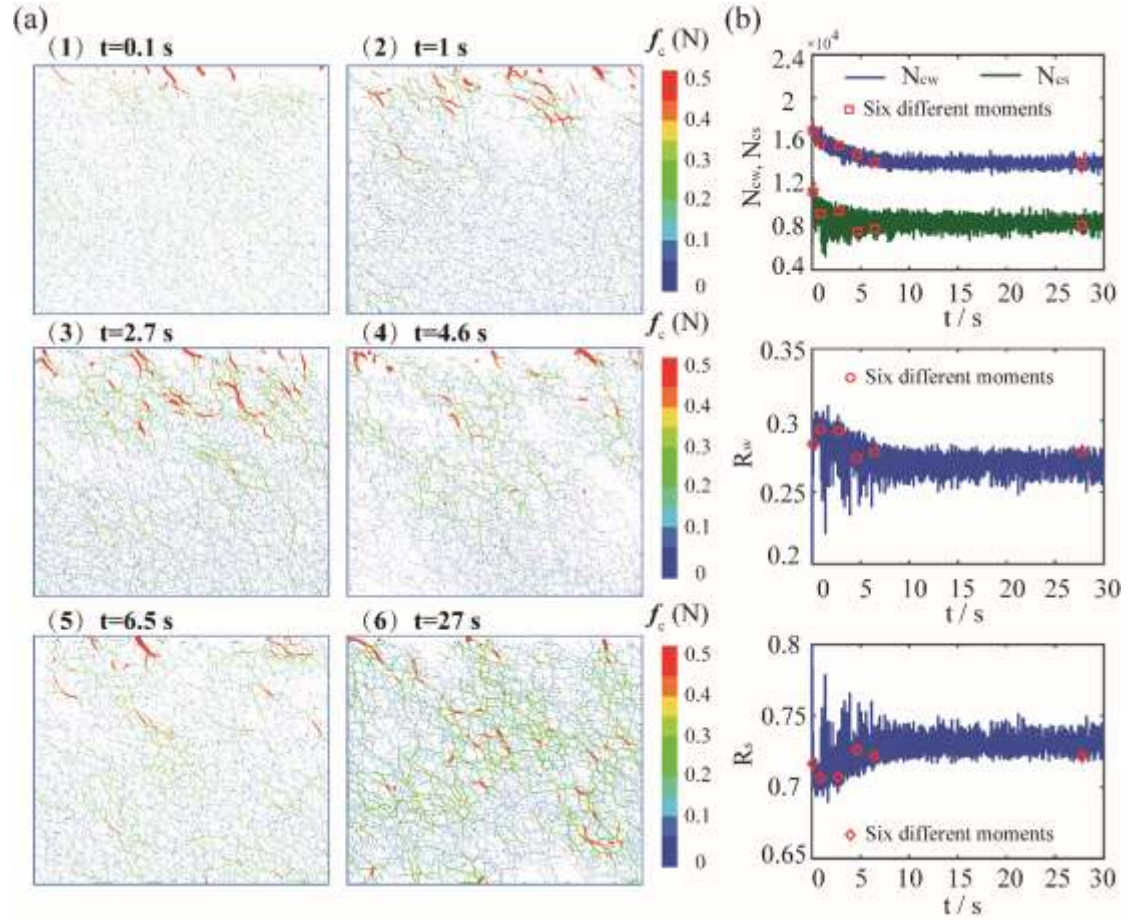


Fig. 6 (a) The contact force network graphs at six different moments under the conditions of $P = 50$ Pa and $V_x = 0.5$ m/s, (b) the time history plots of the strong contact number N_{cs} , the weak contact number N_{cw} , the bearing ratio of strong contacts R_s , and the bearing ratio of weak contacts R_w

Additionally, in order to compare the load-bearing capacities, the bearing ratios of strong contacts and weak contacts, R_s and R_w , respectively, are incorporated. R_s is calculated by using the sum of the strong contact forces divided by the sum of all contact forces, given as $R_s = \frac{\sum_{c \in s} f_c}{\sum f_c}$, where $c \in s$ represents the collection of the strong contacts, and $R_s = 1.0 - R_w$. As shown in Fig. 6(b), the changes in the strong contact number N_{cs} , the weak contact number N_{cw} , R_s , and R_w are quantitatively analyzed. In the evolution process, though the number of weak contacts N_{cw} is always greater than that of strong contacts N_{cs} , the bearing ratio of strong contacts R_s is much greater than that of weak contacts R_w . Moreover, both the number and the bearing ratio of

weak contacts decreases, by contrast, the number of strong contacts also gradually decreases, but the responsible bearing ratio increases.

4.3 Anisotropies in contact and shear strength

Based on the contact force networks in section 4.2, it is ready to deduce the internal shear strength by using the stress-force-fabric relationship. First, the three distribution functions $P(\theta)$, $f_n(\theta)$, and $f_t(\theta)$ are compared between the initial filling state and the steady flow state ($t = 27$ s), as shown in Fig. 7(a). In the initial filling state, $P(\theta)$ is approximately circular as $a_c \cong 0$, indicating that the contact orientations are distributed isotropically. However, the distributions of both the normal and tangential contact forces are anisotropic with $a_n = 0.237$ and $a_t = 0.075$; particularly, the anisotropy in the normal contact force is very strong. At this moment, the force chains are mainly used to carry the applied normal force, but the internal shear strength is relatively weak so that it is easy for the system to flow. As for the steady flow state, both the contact orientations and the contact forces exhibit strong anisotropy. The privileged angles of anisotropy all shift from 0 to θ_1 . Further, as shown in Fig. 7(b), during the continuous shear process, both a_c and a_t increases sharply and then gradually approaches a constant value, but the magnitude of a_t is much smaller than that of a_c . By contrast, a_n increases sharply to a peak but then gradually decreases to a constant value. In the steady state, the ratio of a_c , a_n , and a_t is 15:19:5, implying that the anisotropies in contact orientation and in normal contact force are the main sources of the internal shear strength.

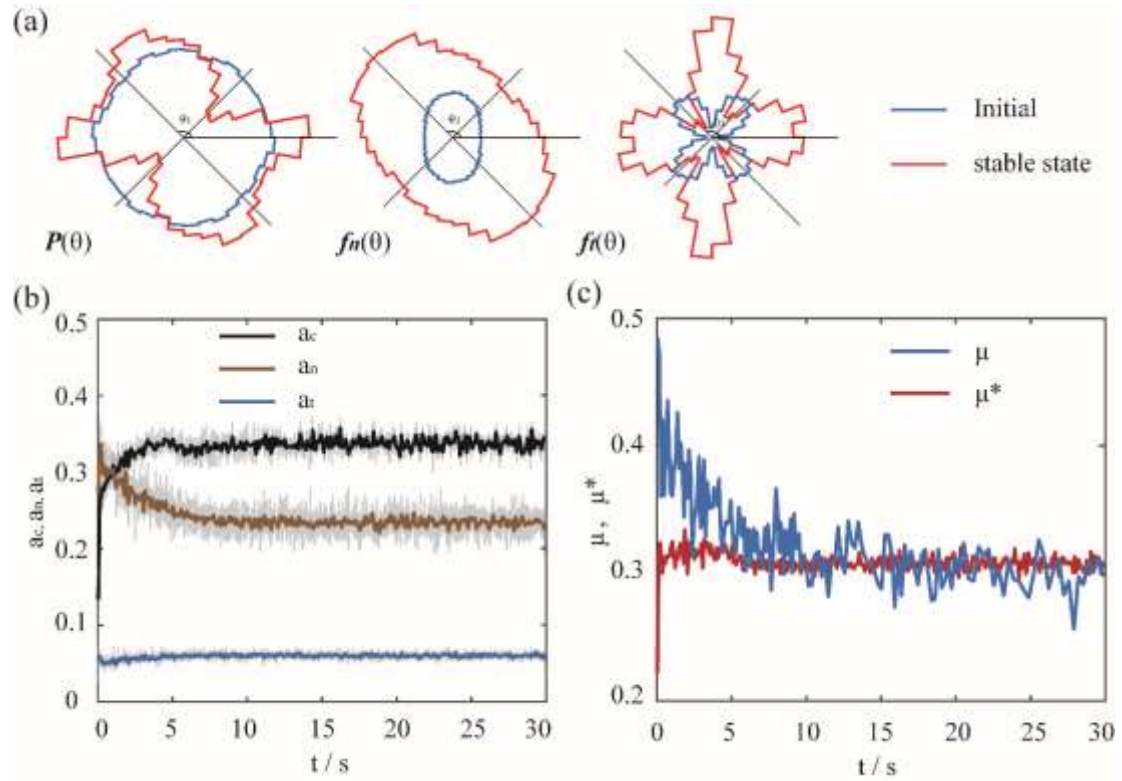


Fig. 7 (a) Three distribution functions $P(\theta)$, $f_n(\theta)$, and $f_t(\theta)$ in polar coordinate system for the initial static and steady flow respectively, (b) time history plots of the anisotropy parameters a_c , a_n , and a_t , (c) the time history plots of the interfacial friction coefficient μ and the internal friction coefficient μ^*

Next, the reasons for the changes in the anisotropy parameters are explained in combination with the system's internal micromechanical behaviors. In the beginning of shear, the increase in a_c and a_n could be attributed to the potential shear resistance caused by the spatial geometric constraints. Nevertheless, most particles except a few ones near the top plate have not undergone shear flow, so the tangential contact force anisotropy parameter a_t changes slightly. Since the horizontal flow is the predominant deformation pattern, the differences in the tangential contact forces are slight, thus a_t is low and has a small contribution to the internal shear strength. Subsequently, because the occurrence of dilatancy reduces the spatial geometric constraints among particles, the original particles which bear large normal contact forces lose lateral support and cannot maintain stability. Once these particles are out of balance, the breakage of the established contacts causes the decrease in a_n . On the other hand, particle flow reduces

the number of contacts especially in the direction of the minimum principal stress, which leads to a gradual increase in the contact number difference between along the direction of the maximum principal stress and along the direction of the minimum principal stress, thus a_c gradually increases. In short, the increase in a_c costs the reduction of a_n , which damages the system's stability.

The internal friction coefficient μ^* is obtained according to Equation 3, as shown in Fig. 7(c). It is found that μ^* first rapidly increases to the peak, and then gradually drops to a fixed value. By comparison, it is evident that the evolution trends are opposite between the internal friction coefficient μ^* and the interfacial friction coefficient μ . Moreover, μ is greater than μ^* until approximately equal in the steady flow state. Therefore, the flow evolution from static to stable flow under continuous shear, is essentially realized by achieving the final dynamic balance between the boundary drive strength and the internal shear strength.

5. Effects of shear velocity on rheological properties

5.1 Effects of shear velocity on the transient flow state

Fig. 8 shows the changes of the dimensionless flow region DH_F and the expansion of the top plate's height φ with time under four different velocities. The evolution profiles of the horizontal velocity at other velocities are similar to that of $V_x = 0.5$ m/s. Besides, three distinct stages, i.e., transmission (T), adjustment (A), and stabilization (S) are identified for all the velocities. However, an increase in the shear velocity strengthens the inertial effect and weakens the microscopic particle rearrangement, thus reduces the time required for the system achieving a global flow. For example, as shown in Figs. 8(a), because the microscopic rearrangement is very significant at $V_x = 0.1$ m/s, the time required for DH_F increasing from 0 to 1 is about 20 s, which is much longer compared with the other velocities. On the other hand, as shown in Fig. 8(b), the maximum expansion in height, i.e., the dilatancy extent, increases with shear velocity. Similarly, at higher velocity, the system requires less time to reach the

maximum expansion. Therefore, the shear velocity does not affect the evolution characteristics of particle flow, but changes the momentum transfer rate.

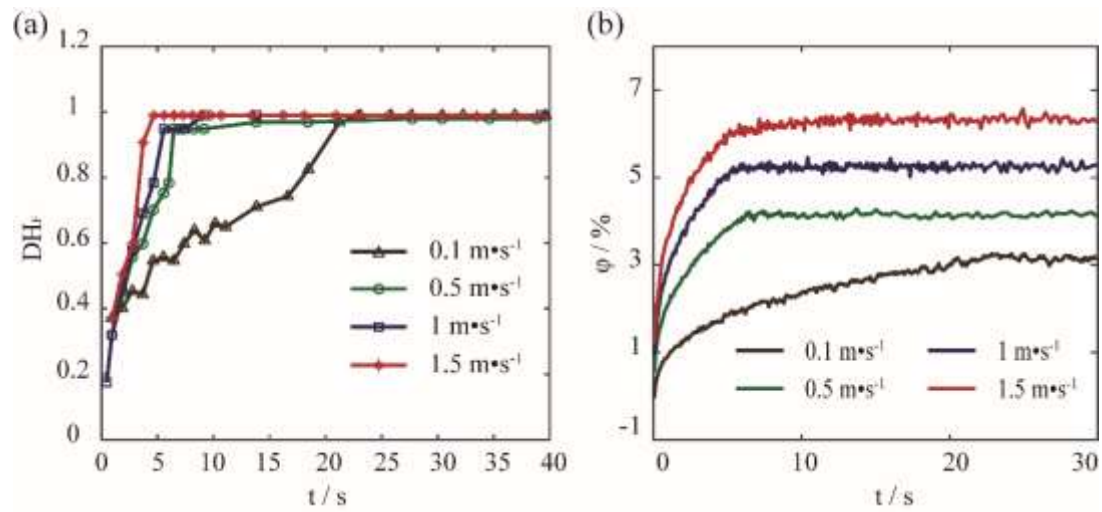


Fig. 8 The changes of the dimensionless flow region DH_F (a), and the expansion of the top plate's height φ (b) with time under four different velocities

5.2 Effects of shear velocity on interfacial friction coefficient and shear strength

As shown in Figs. 9(a) - 9(c), with shear velocity increasing, the magnitude of F_T at the same moment significantly increases while F_N always fluctuates around 10 N, so that the interfacial friction coefficient μ raises as well. This could be explained by that when the overall horizontal flow velocity increases, the boundary drive strength must be improved correspondingly, in order to overcome more energy dissipation and maintain the stable flow. Additionally, the simulation results fluctuate more intensively with the increase of shear velocity.

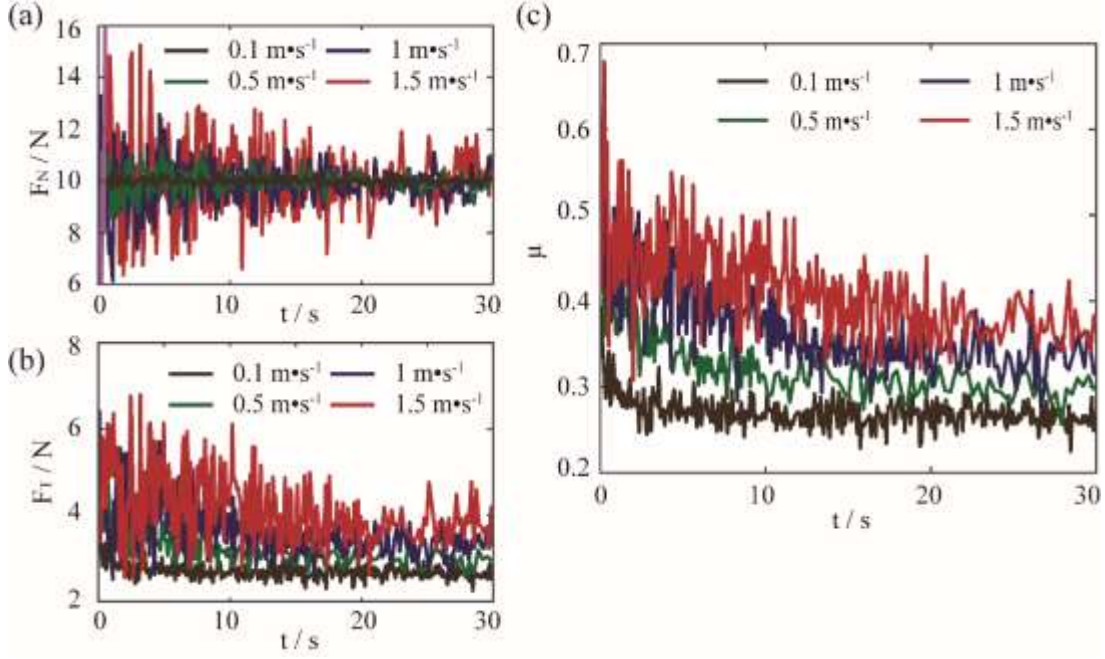


Fig. 9 The changes of F_N (a), F_T (b), and μ (c) with time under four different velocities

The anisotropy parameters a_c , a_n , and a_t all increase with shear velocity as shown in Figs. 10(a)-10(c). According to Equation (3), the system's internal shear strength characterized by μ^* is improved correspondingly in Fig. 10(d). The changes in these anisotropy parameters could be explained by comparing the contact force network graphs in the steady state. As shown in Fig. 11(a), at $V_x = 0.1$ m/s, a dense and continuous force chain network is formed as the particles remain in contact and interact frictionally with neighbors over long durations. By contrast, at $V_x = 1.5$ m/s, the distribution of contact forces is so dispersed that only some local force chain segments exist. As a result, the contact number difference increases between along the maximum principal stress and along the minimum principal stress, leading to an increase in the contact orientation anisotropy parameter a_c . As shown in Fig. 11(b), in the steady state, both the strong contact number N_{cs} and the weak contact number N_{cw} decrease with shear velocity. Additionally, with shear velocity increasing, the bearing ratio of weak contacts R_w decreases while the bearing ratio of strong contacts R_s increases, so the differences in the force magnitudes become more distinct, which explains the increase in the anisotropy parameters of contact forces a_n and a_t .

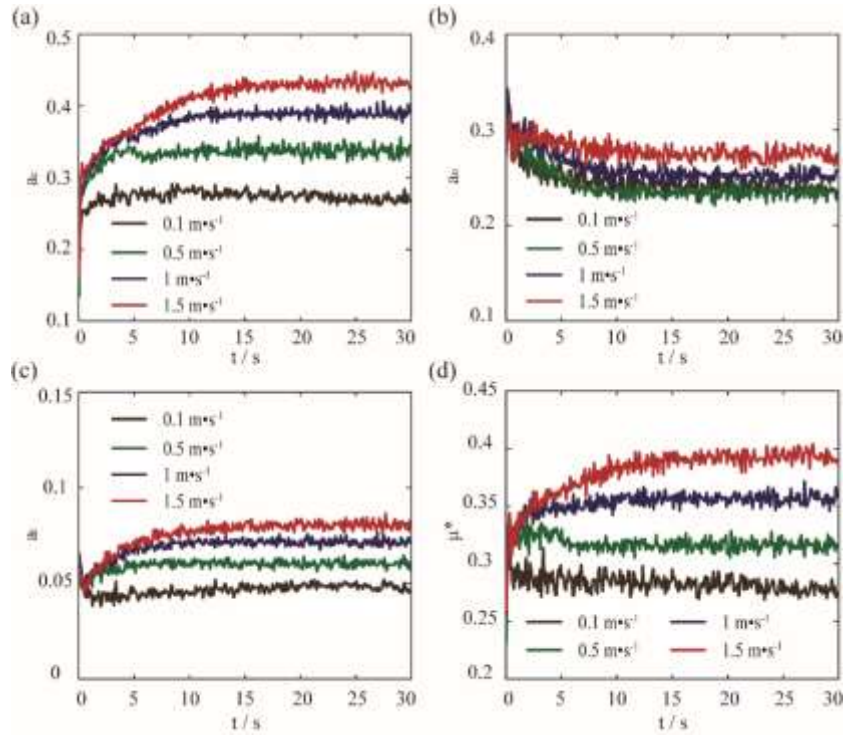


Fig. 10 The changes of a_c (a), a_n (b), a_t (c), and μ^* (d) with time under four different velocities

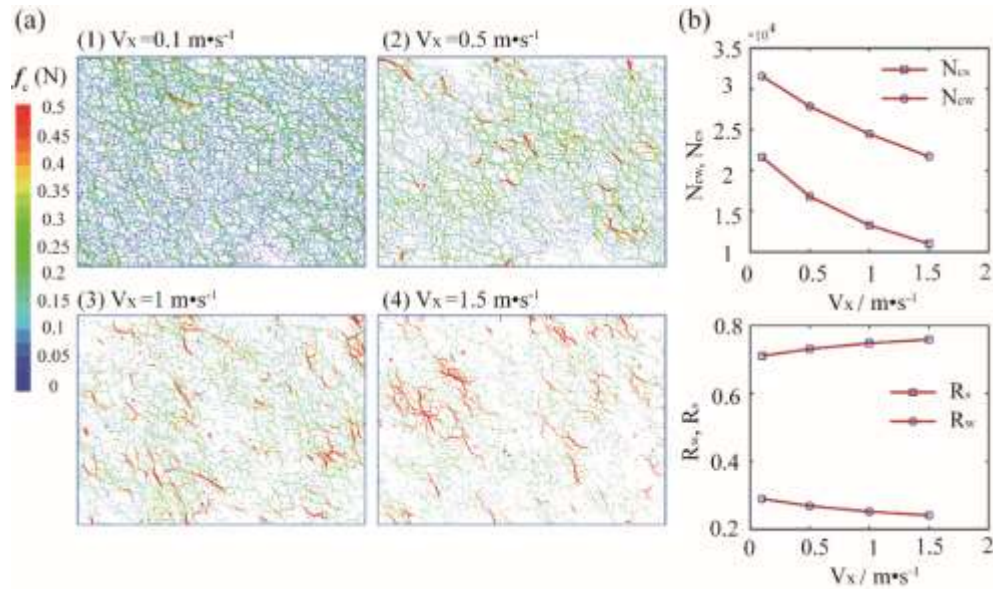


Fig. 11 (a) In the steady state, the contact force network graphs under different shear velocities, (b) the strong contact number N_{CS} , the weak contact number N_{CW} , the bearing ratio of strong contacts R_S , and the bearing ratio of weak contacts R_W as a function of the shear velocity

In the steady flow state, the stable interfacial friction coefficient μ is equal with the internal friction coefficient μ^* , unified as the effective friction coefficient μ_e . Numerous experimental and simulation results have confirmed that, in the inertia regime, the effective friction coefficient μ_e monotonically increases while the solid fraction ε monotonically decreases, as a function of the inertia number I , given as:

$$\mu_e(I) = \mu_i + a_\mu I^{b_\mu} \quad (4)$$

$$\varepsilon(I) = \varepsilon_i - a_\varepsilon I^{b_\varepsilon} \quad (5)$$

where μ_i , a_μ , b_μ , ε_i , a_ε , and b_ε are constants. In Fig. 12(a), our simulation results can be well fitted using $\mu_e(I) = 0.26 + 0.61I^{0.74}$ and $\varepsilon(I) = 0.81 - 0.19I^{0.84}$, which form the constitutive laws for the dense granular material under plane shear in this study.

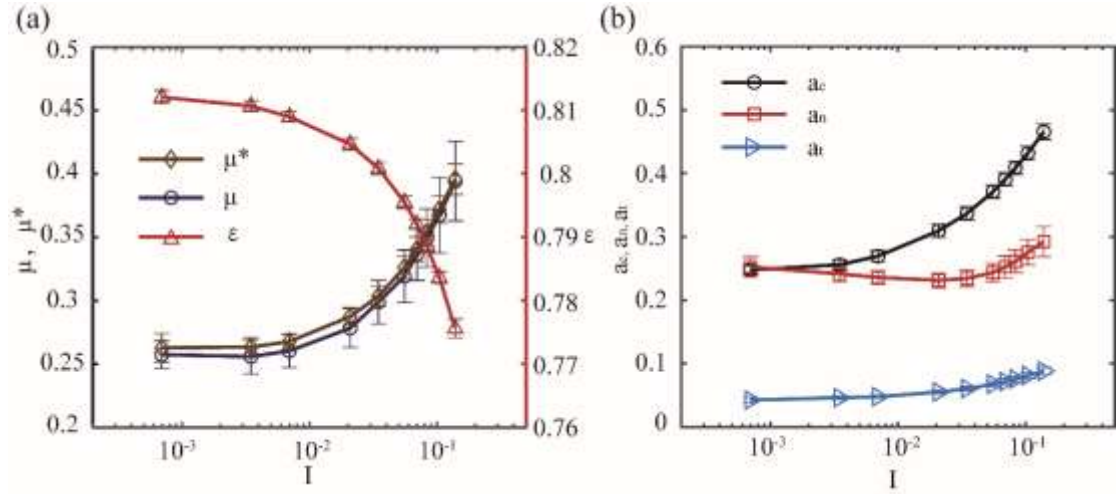


Fig. 12 (a) The interfacial friction coefficient μ , the internal friction coefficient μ^* and the solid fraction ε in the steady state, and (b) the variations of the anisotropy parameter a_c , a_n , and a_t as a function of the inertial number I

Furthermore, Fig. 12(b) shows the variations of the anisotropy parameters with the inertial number I . To be specific, the contact orientation anisotropy parameter a_c increases significantly from 0.25 to 0.50, and the normal contact force anisotropy parameter a_n first slightly decreases but then gradually increases to 0.30, while the

tangential contact force anisotropy parameter a_t only slightly increases from 0.05 to 0.10. By comparing their increasing extents, it can be concluded that a_c and a_n are the main sources of the system's shear strength. Moreover, the contribution of a_c becomes more predominant with the increase of the inertia number I .

6. Conclusions

DEM simulations are employed to investigate the transient rheological properties of a dense granular system under plane shear in the inertial regime. Simulation results show that there are three typical stages in the evolution process of the system's horizontal flow state, namely, transmission, adjustment, and stabilization. The shear dilatancy which is caused by the vertical movement of particles, weakens the system's tangential load-bearing capacity, decreases the interfacial friction coefficient μ and reduces the boundary drive strength. On the other hand, the variations in the anisotropies of contact orientation and contact forces, increase the internal friction coefficient μ^* and improve the system's shear strength. As a result, the evolution trends are opposite between μ and μ^* . Therefore, the flow evolution from static to stable flow is essentially realized by achieving the final dynamic balance between the boundary drive strength and the internal shear strength. An increase in the shear velocity enhances the rheological evolution rate, but the evolution pattern is not changed. Distinguished from the micromechanical behaviors, under different shear velocities the system's shear strength always mainly stems from the anisotropies in contact orientation and in normal contact force. Moreover, the anisotropy in contact orientation contributes more with the increase of shear velocity.

Our work would help elucidate the shear equilibrium mechanism for dense granular flow and explain the dependences of rheological constitutive laws on the flow state. In the future, we would conduct a systematic analysis on the evolution of contact and contact forces for exploring the internal microscopic mechanical properties.

Declarations

Funding This work was financially supported by the National Natural Science Foundation of China Grant Nos. 51975174 and 51875154.

Conflict of interest The authors declare that they have no conflict of interests.

Availability of data and material The data presented in this study are available on request from the corresponding author.

Code availability The DEM codes are available on request from the corresponding author.

References

- [1] Forterre, Y., Pouliquen, O.: Flows of dense granular media. *Annu Rev Fluid Mech.* 40,1-24 (2008)
- [2] Andreotti, B., Forterre, Y., Pouliquen, O.: Granular media: between fluid and solid. Cambridge University Press (2013)
- [3] Zhang, Y., Campbell, C. S.: The interface between fluid-like and solid-like behaviour in two-dimensional granular flows. *J Fluid Mech.* 237,541-568 (1992)
- [4] Lherminier, S., Planet, R., dit Vehel, V. L., Simon, G., Vanel, L., Måløy, K. J., Ramos, O.: Continuously sheared granular matter reproduces in detail seismicity laws. *Phys Rev Lett.* 122,218501 (2019)
- [5] Zhang, H., Liu, S., Xiao, H.: Sliding friction of shale rock on dry quartz sand particles. *Friction.* 7,307-315 (2019)
- [6] Scholz, C. H.: Earthquakes and friction laws. *Nature.* 391,37 (1998)
- [7] Iordanoff, I., Khonsari, M.: Granular lubrication: toward an understanding of the transition between kinetic and quasi-fluid regime. *J Tribol.* 126,137-145 (2004)
- [8] Ciamarra, M. P., Dalton, F., de Arcangelis, L., Godano, C., Lippiello, E., Petri, A.: The role of interstitial impurities in the frictional instability of seismic fault models. *Tribology Letters.* 48,89-94 (2012)
- [9] Wang, W., Liu, X., Xie, T., Liu, K.: Effects of sliding velocity and normal load on tribological characteristics in powder lubrication. *Tribology Letters.* 43,213-219 (2011)
- [10] Singla, N., Brunel, J.-F., Mège-Revil, A., Kasem, H., Desplanques, Y.: Experiment to investigate the relationship between the third-body layer and the occurrence of squeals in dry sliding contact. *Tribology Letters.* 68,1-11 (2020)
- [11] MiDi, G.: On dense granular flows. *Euro Phys J E.* 14,341-365 (2004)
- [12] Fannon, J. S., Moyles, I. R., Fowler, A. C.: Application of the compressible $\mu(I)$ -dependent rheology to chute and shear flow instabilities. *J Fluid Mech.* 864,1026-1057 (2019)
- [13] Azéma, E., Radjai, F., Roux, J.-N.: Inertial shear flow of assemblies of frictionless polygons: Rheology and microstructure. *Euro Phys J E.* 41,2 (2018)

- [14] Chialvo, S., Sun, J., Sundaresan, S.: Bridging the rheology of granular flows in three regimes. *Phys Rev E*. 85,021305 (2012)
- [15] Bagnold, R. A.: The shearing and dilatation of dry sand and the 'singing' mechanism. *Proceedings of the Royal Society of London Series A Mathematical and Physical Sciences*. 295,219-232 (1966)
- [16] Lemaître, A.: Rearrangements and dilatancy for sheared dense materials. *Phys Rev Lett*. 89,195503 (2002)
- [17] Bandi, M. M., Das, P., Gendelman, O., Hentschel, H. G. E., Procaccia, I.: Universal scaling laws for shear induced dilation in frictional granular media. *Granular Matter*. 21,40 (2019)
- [18] Thompson, P. A., Grest, G. S.: Granular flow: friction and the dilatancy transition. *Phys Rev Lett*. 67,1751 (1991)
- [19] Azéma, E., Radjai, F.: Internal structure of inertial granular flows. *Phys Rev Lett*. 112,078001 (2014)
- [20] Jop, P.: Rheological properties of dense granular flows. *CR Phys*. 16,62-72 (2015)
- [21] Da Cruz, F., Emam, S., Prochnow, M., Roux, J.-N., Chevoir, F.: Rheophysics of dense granular materials: Discrete simulation of plane shear flows. *Phys Rev E*. 72,021309 (2005)
- [22] Fall, A., Ovarlez, G., Hautemayou, D., Mézière, C., Roux, J.-N., Chevoir, F.: Dry granular flows: Rheological measurements of the μ (I)-rheology. *Journal of rheology*. 59,1065-1080 (2015)
- [23] Schaeffer, D., Barker, T., Tsuji, D., Gremaud, P., Shearer, M., Gray, J.: Constitutive relations for compressible granular flow in the inertial regime. *J Fluid Mech*. 874,926-951 (2019)
- [24] Divoux, T., Géminard, J.-C.: Friction and dilatancy in immersed granular matter. *Phys Rev Lett*. 99,258301 (2007)
- [25] Chevoir, F., Roux, J.-N., da Cruz, F., Rognon, P. G., Koval Jr, G.: Friction law in dense granular flows. *Powder Technology*. 190,264-268 (2009)
- [26] Tang, Z., Brzinski, T. A., Shearer, M., Daniels, K. E.: Nonlocal rheology of dense granular flow in annular shear experiments. *Soft matter*. 14,3040-3048 (2018)

- [27] Mitchell, J. K., Soga, K.: Fundamentals of soil behavior. John W., Sons, Canada (2005)
- [28] Koval, G., Roux, J.-N., Corfdir, A., Chevoir, F.: Annular shear of cohesionless granular materials: From the inertial to quasistatic regime. *Phys Rev E*. 79,021306 (2009)
- [29] Binaree, T., Azéma, E., Estrada, N., Renouf, M., Preechawuttipong, I.: Combined effects of contact friction and particle shape on strength properties and microstructure of sheared granular media. *Phys Rev E*. 102,022901 (2020)
- [30] Azéma, É., Radjai, F., Roux, J.-N.: Internal friction and absence of dilatancy of packings of frictionless polygons. *Phys Rev E*. 91,010202 (2015)
- [31] Estrada, N., Azéma, E., Radjai, F., Taboada, A.: Identification of rolling resistance as a shape parameter in sheared granular media. *Phys Rev E*. 84,011306 (2011)
- [32] Koval, G., Chevoir, F., Roux, J.-N., Sulem, J., Corfdir, A.: Interface roughness effect on slow cyclic annular shear of granular materials. *Granular Matter*. 13,525-540 (2011)
- [33] Siavoshi, S., Orpe, A. V., Kudrolli, A.: Friction of a slider on a granular layer: Nonmonotonic thickness dependence and effect of boundary conditions. *Phys Rev E*. 73,010301 (2006)
- [34] Trulsson, M., DeGiuli, E., Wyart, M.: Effect of friction on dense suspension flows of hard particles. *Phys Rev E*. 95,012605 (2017)
- [35] Meng, F., Liu, H., Hua, S., Pang, M.: Experimental Research on Sliding Friction of Dense Dry Particles Lubricated Between Parallel Plates. *Tribology Letters*. 69,1-14 (2021)
- [36] Zhang, X., Sun, W., Wang, W., Liu, K.: Experimental investigation of granular friction behaviors during reciprocating sliding. *Friction*. 1-16 (2021).<https://doi.org/10.1007/s40544-021-0488-2>
- [37] Kuwano, O., Ando, R., Hatano, T.: Crossover from negative to positive shear rate dependence in granular friction. *Geophys Res Lett*. 40,1295-1299 (2013)
- [38] Degiuli, E., Mcelwaine, J. N., Wyart, M.: Phase diagram for inertial granular flows. *Phys Rev E*. 94,012904 (2016)

- [39] Hatano, T.: Power-law friction in closely packed granular materials. *Phys Rev E*. 75,060301 (2007)
- [40] Boyer, F., Guazzelli, É., Pouliquen, O.: Unifying suspension and granular rheology. *Phys Rev Lett*. 107,188301 (2011)
- [41] Berger, N., Azéma, E., Douce, J.-F., Radjai, F.: Scaling behaviour of cohesive granular flows. *EPL (Europhysics Letters)*. 112,64004 (2016)
- [42] Wu, W., Ma, G., Zhou, W., Wang, D., Chang, X.: Force transmission and anisotropic characteristics of sheared granular materials with rolling resistance. *Granular Matter*. 21,88 (2019)
- [43] Majmudar, T. S., Behringer, R. P.: Contact force measurements and stress-induced anisotropy in granular materials. *Nature*. 435,1079-1082 (2005)
- [44] Sufian, A., Russell, A., Whittle, A.: Anisotropy of contact networks in granular media and its influence on mobilised internal friction. *Géotechnique*. 67,1067-1080 (2017)
- [45] Zhang, J., Majmudar, T., Tordesillas, A., Behringer, R.: Statistical properties of a 2D granular material subjected to cyclic shear. *Granular Matter*. 12,159-172 (2010)
- [46] Mollon, G.: Solid flow regimes within dry sliding contacts. *Tribology Letters*. 67,1-20 (2019)
- [47] Voivret, C., Radjai, F., Delenne, J.-Y., El Youssoufi, M. S.: Multiscale force networks in highly polydisperse granular media. *Phys Rev Lett*. 102,178001 (2009)
- [48] Azéma, E., Linero, S., Estrada, N., Lizcano, A.: Shear strength and microstructure of polydisperse packings: The effect of size span and shape of particle size distribution. *Phys Rev E*. 96,022902 (2017)
- [49] Cantor, D., Azéma, E., Sornay, P., Radjai, F.: Rheology and structure of polydisperse three-dimensional packings of spheres. *Phys Rev E*. 98,052910 (2018)
- [50] Pena, A., Garcia-Rojo, R., Herrmann, H. J.: Influence of particle shape on sheared dense granular media. *Granular Matter*. 9,279-291 (2007)
- [51] Azéma, E., Estrada, N., Radjai, F.: Nonlinear effects of particle shape angularity in sheared granular media. *Phys Rev E*. 86,041301 (2012)
- [52] Azéma, E., Radjai, F., Dubois, F.: Packings of irregular polyhedral particles:

- strength, structure, and effects of angularity. *Phys Rev E*. 87,062203 (2013)
- [53] Botton, M., Azéma, E., Estrada, N., Radjai, F., Lizcano, A.: Quasistatic rheology and microstructural description of sheared granular materials composed of platy particles. *Phys Rev E*. 87,032206 (2013)
- [54] Botton, M., Estrada, N., Azéma, E., Radjai, F.: Particle alignment and clustering in sheared granular materials composed of platy particles. *Euro Phys J E*. 37,116 (2014)
- [55] Vo, T.-T.: Rheology and granular texture of viscoinertial simple shear flows. *Journal of Rheology*. 64,1133-1145 (2020)
- [56] Chèvremont, W., Chareyre, B., Bodiguel, H.: Quantitative study of the rheology of frictional suspensions: Influence of friction coefficient in a large range of viscous numbers. *Physical Review Fluids*. 4,064302 (2019)
- [57] Macaulay, M., Rognon, P.: Viscosity of cohesive granular flows. *Soft matter*. 17,165-173 (2021)
- [58] Shojaaee, Z., Roux, J.-N., Chevoir, F., Wolf, D. E.: Shear flow of dense granular materials near smooth walls. I. Shear localization and constitutive laws in the boundary region. *Phys Rev E*. 86,011301 (2012)
- [59] Cundall, P. A., Strack, O. D.: A discrete numerical model for granular assemblies. *geotechnique*. 29,47-65 (1979)
- [60] Fillot, N., Iordanoff, I., Berthier, Y.: Modelling third body flows with a discrete element method—a tool for understanding wear with adhesive particles. *Tribology International*. 40,973-981 (2007)
- [61] Roux, J.-N., Combe, G.: Quasistatic rheology and the origins of strain. *CR Phys*. 3,131-140 (2002)
- [62] Rothenburg, L., Bathurst, R.: Analytical study of induced anisotropy in idealized granular materials. *Geotechnique*. 39,601-614 (1989)

Supplementary Files

This is a list of supplementary files associated with this preprint. Click to download.

- [GraphicalAbstract.tif](#)